ADVANCED MATERIALS
www.advmat.de

Electron-Assisted Generation and Straight Movement of Skyrmion Bubble in Kagome $TbMn_6Sn_6$

Zhuolin Li, Qiangwei Yin, Wenxin Lv, Jun Shen, Shouguo Wang, Tongyun Zhao, Jianwang Cai, Hechang Lei, Shi-Zeng Lin, Ying Zhang, and Baogen Shen*

Topological magnetic textures are promising candidates as binary data units for the next-generation memory device. The precise generation and convenient control of nontrivial spin topology at zero field near room temperature endows the critical advantages in skyrmionic devices but is not simultaneously integrated into one material. Here, in the Kagome plane of quantum $TbMn_6Sn_6$, the expedient generation of the skyrmion bubbles in versatile forms of lattice, chain, and isolated one by converging the electron beam, where the electron intensity gradient contributes to the dynamic generation from local anisotropy variation near spin reorientation transition (SRT) is reported. Encouragingly, by utilizing the dynamic shift of the SRT domain interface, the straight movement is actualized with the skyrmion bubble slave to the SRT domain interface forming an elastic composite object, avoiding the usual deflection from the skyrmion Hall effect. The critical contribution of the SRT domain interface via conveniently electron-assisted heating is further theoretically validated in micromagnetic simulation, highlighting the compatible application possibility in advanced devices.

1. Introduction

Magnetic nano-domains with nontrivial topology, such as skyrmions and skyrmion bubbles, have aroused intensive studies due to their intriguing properties and potential applications in future memory devices.[1–3] These topologically nonlinear spin textures are primarily stabilized in symmetry-lacking systems, including interfacial symmetry broken multilayers and chiral bulk crystals based on the Dzyaloshinskii–Moriya interaction (DMI) mechanism.[4–6] Alternatively, other magnetic interactions like dipole–dipole interaction (DDI),[7,8] Ruderman–Kittel–Kasuya–Yosida,[9–11] or frustrated interactions[12–14] can also determine the generation of skyrmionic structures. Based on current skyrmion progress, searching for field-free topological configurations and convenient manipulation methods at room temperature would be a breakthrough to promote future applications in spintronic devices.

External beam stimuli such as laser, synchrotron X-rays, and electron beams have demonstrated the capability to generate skyrmions near T_c,[15–18] but the intricate requirements of special sample fabrication techniques or polarized probing tips are not good to practical applications. Instead, the interesting interactions of electrons

Z. Li, T. Zhao, J. Cai, Y. Zhang, B. Shen
Beijing National Laboratory for Condensed Matter Physics
Institute of Physics
Chinese Academy of Sciences
Beijing 100190, China
E-mail: zhangy@iphy.ac.cn

Z. Li, T. Zhao, J. Cai, Y. Zhang, B. Shen
School of Physical Sciences
University of Chinese Academy of Sciences
Beijing 101408, China

Q. Yin, W. Lv, H. Lei
Department of Physics and Beijing Key Laboratory of Optoelectronic Functional Materials & MicroNano Devices
Renmin University of China
Beijing 100872, China

Q. Yin, W. Lv, H. Lei
Key Laboratory of Quantum State Construction and Manipulation (Ministry of Education)
Renmin University of China
Beijing 100872, China

The ORCID identification number(s) for the author(s) of this article can be found under https://doi.org/10.1002/adma.202309538

DOI: 10.1002/adma.202309538

J. Shen
Department of Energy and Power Engineering
School of Mechanical Engineering
Beijing Institute of Technology
Beijing 100081, China

S. Wang
Anhui Key Laboratory of Magnetic Functional Materials and Devices
School of Materials Science and Engineering
Anhui University
Hefei 230601, China

S.-Z. Lin
Theoretical Division and Center for Integrated Nanotechnologies
Los Alamos National Laboratory
Los Alamos
New Mexico 87545, USA

Y. Zhang
Open Access Research Infrastrucure
Songshan Lake Materials Laboratory
Dongguan, Guangdong 523808, China

B. Shen
Ningbo Institute of Materials Technology & Engineering
Chinese Academy of Sciences
Ningbo, Zhejiang 315201, China

with topological magnetic textures by using convenient electric manipulation[19–21] anticipate perspective application in next-generation skyrmionic devices because of the good compatibility, low energy consumption, and high speed.[22–24] As for the information transportation by driving the topological skyrmion in ferromagnetic devices like race track memory, the significant pinning effects for relatively small-size skyrmions and the usual deflection from skyrmion Hall effect[25–28] become the big challenge. Numerous tentative studies such as confining skyrmions in the track with spatially tailored DMI,[29] exploiting the domain wall constraints,[30] using surface acoustic wave modulation,[31] driving skyrmions through temperature gradient[32] and searching for ferrimagnets[33] or synthetic antiferromagnets[34–36] have been conducted but without observing the high-efficient skyrmion movement at room temperature so far.

Recently, Kagome magnets draw great attention due to the recently-discovered versatile nontrivial properties, such as dispersionless flat band,[37–39] and topological electronics, in combination with frustrated magnetism and spin–orbit coupling, which could induce chiral anomalies, large anomalous Hall effect and unique behavior of magnetic topological excitations.[40–43] Therefore, it is highly anticipated to explore nontrivial spin textures in the frustrated Kagome plane of quantum magnet $TbMn_6Sn_6$.

In this work, skyrmion bubbles have been successfully generated and driven in the Kagome plane of the $TbMn_6Sn_6$ by using two kinds of convenient electron-assisted heating sources in Lorentz transmission electron microscopy (L-TEM). The induced electron intensity gradient via converging electron beam contributes to the dynamic skyrmion bubble lattice generation from the local anisotropy variation across the spin reorientation transition (SRT) domain interface, where both the skyrmion bubble chain and isolated skyrmion bubble have also been obtained in a confined structure without the requirement of any external field. More strikingly, by subsequently utilizing the dynamic shift of the SRT domain interface, the skyrmion bubble slaved to the interface as an elastic composite object can be simultaneously driven along the straight line, avoiding the significant deflection from the skyrmion Hall effect. The corresponding micromagnetic simulation further confirms the critical contribution of local anisotropy change near SRT and the dipole–dipole repulsion in generating and activating the skyrmion bubble.

2. Results and Discussion

2.1. The Skyrmion Lattice Generation from Dynamic Anisotropy Variation near SRT Induced by Converging Electron Beam

The pure single crystal structure is confirmed in $TbMn_6Sn_6$ (Note S1, Supporting Information) with centrosymmetric P6/mmm space group and stacking of the hexagonal Tb layer and the Kagome Mn planes along the *c*-axis[44,45] (**Figure 1a**). Temperature-dependent magnetic susceptibility $\chi(T)$ (Figure 1b) shows opposite changes of susceptibility along the H//b and H//c axes respectively, demonstrating an abrupt SRT jump with anisotropy from the *c*-axis to *a–b* plane upon increasing temperature over $T_{sr} = 310$ K. The corresponding domain evolution across SRT is clearly demonstrated by a series of L-TEM images acquired in the Kagome plane of $TbMn_6Sn_6$ while gradually heating up (Figure S2a–c, Supporting Information), where a prominent domain interface between perpendicular stripes with *c*-axis (out-of sample plane) magnetization to 180° domains with *a–b* plane (in sample plane) magnetization is observed near room temperature. The slight transition temperature difference of ≈10 K lower than the bulk measured in the physical property measurement system is induced by the dipolar energy difference from sample thickness. The near room temperature SRT guarantees that the anisotropy transition could be induced by small external energy like a convenient electron beam (Figure S2d–f, Supporting Information).

A low perpendicular magnetic field of 500 Oe, which is not high enough to change the stripe domain state, is applied to stabilize the skyrmions with a certain polarization during electron beam manipulation (Figure 1d). Strikingly, skyrmion bubbles (Type I bubbles with a topological number of ±1[46–48]) in the form of a closely packed lattice (Figure 1e–g) are generated from multiple converging electron beams on these stripe domains. The chirality of generated skyrmion bubbles is preferentially fixed at one direction with occasional coexistence of different chirality. Here, the centrosymmetric crystal structure of $TbMn_6Sn_6$ forbids the DMI,[42,46,49] and the skyrmion bubble is stabilized by the competition of the multiple magnetic interactions including exchange couplings, DDI, perpendicular anisotropy, and Zeeman coupling due to external fields. It should be noted that the generated lattice can sustain at room temperature after the external field is removed.

To stress the critical contribution of the electron intensity gradient in generating skyrmion bubbles, we conducted a homogeneous heating experiment under a uniform low-intensity electron beam. The skyrmion bubble phase is not achieved by varying the magnetic field and the temperature (Note S3, Supporting Information), although this homogenous condition could generate skyrmions in other materials.[8,7,50] Furthermore, we find that the incident electron energy for the converged electron beam is equivalent to the current density ≈10^5 A m^{-2},[51,52] which is too low to alter the magnetization state via the spin transfer torque (STT) effect.[53,54] These results confirm the special contribution of converged electrons in producing the inhomogeneous gradient with a temperature higher than T_{sr} at the beam center and lower in the surrounding region. Thus, the SRT domain interface between the *c*-axis and *a–b* plane magnetization is prone to nucleate the skyrmion bubble in the local sample region as schematically shown in Figure 1c. Dynamically, the corresponding oscillation of the domain interface due to the energy fluctuation (Video S1, Supporting Information) plays a critical role in squeezing out the skyrmion bubble from stripe domains. Additional repulsive force due to the confinement from the surrounding rigid stripe domain also contributes to the squeezing-out process and stability of skyrmion bubbles after removing the external field. This dynamic process helps to understand why the homogeneous thermal equilibrium state (Figures S3,S4, Supporting Information) is unable to generate skyrmion bubbles. Therefore, an electron beam could be used as a convenient heating source to generate skyrmions with near room temperature SRT, which is difficult for the material with SRT away from room temperature.[55–58]

The effect of converging electrons is modeled by alternating the *c*-axis and *a–b* plane anisotropy in a local specified region in the micromagnetic simulation with a stripe domain as the initial

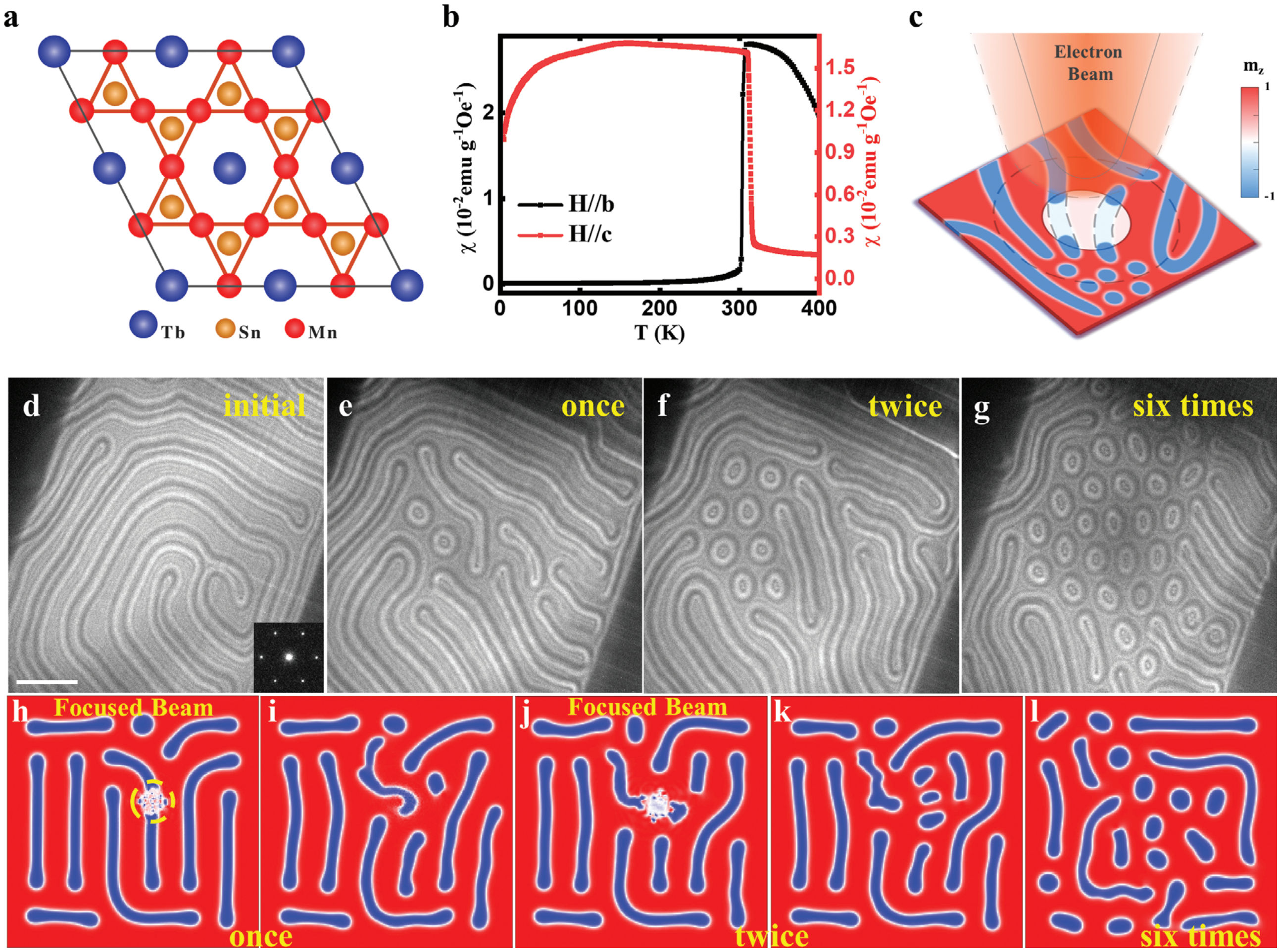

Figure 1. Skyrmion bubble lattice generated from converging electron beam under low magnetic field in the Kagome plane of $TbMn_6Sn_6$. a) Schematic structure of Kagome plane with hexagonal R layer and Kagome Mn planes stacked along the *c-axis* in the sequence of Mn-Tb-Mn-Mn-Tb-Mn. b) Temperature-dependent magnetic susceptibility $\chi(T)$ for zero-field cooling along the *b*- and *c*-axis, respectively, depicting the SRT magnetization transition near 310 K. c) Schematic illustration for the skyrmion bubble generation during magnetization change from out-of-plane to in-plane upon converging the electron beam on the central white region. d–g) Domain evolution from initial stripes to skyrmion bubble lattice after repeatedly converging electron beam. The inset shows the electron diffraction patterns of the Kagome plane. h–l) Corresponding micromagnetic simulation including the first time converging (h) and diverging (i) electron beam, the second time converging (j) and diverging (k), and six times' operations (l) at a magnetic field of 500 Oe. The yellow dotted circle marks the position of the local converged electron area.

ground state. Although MuMax^3 is the preferential tool in recent studies,[59] here, the simulations are performed with the standard object-oriented micromagnetic framework (OOMMF) extensible solver (OXS)[60] based on our accumulated experiences. Under a low magnetic field, the skyrmion bubbles are squeezed out from the SRT domain interface with local anisotropy change from *c*-axis to *a*–*b* plane on the specific stripe region (yellow dotted circle in Figure 1h). Interestingly, after turning off the anisotropy difference to mimic diverging the electron beam, the generated skyrmion bubbles remain isolated (Figure 1i,k) due to the automatically added DDI corresponding to the stripe domain confinement. More and more skyrmion bubbles are generated by repeating the operation until the complete skyrmion bubble lattice state (Figure 1j–l). The consistency between the experimental and simulation results confirms the effectiveness of utilizing the local SRT domain interface to generate skyrmion bubbles from stripe domains.

2.2. Zero-Field Skyrmion Bubble Chain and Isolated Skyrmion Bubble via Additional Edge Confinement

We further strengthen the confinement effects by fabricating a narrow device with rigid edges on both sides. By converging the electron beam under the same low magnetic field of 500 Oe, similar skyrmion bubble generation is observed together with the extending of the SRT domain interface to the other side of the stripe as schematically illustrated in **Figure 2a**. The comparable size between the skyrmion bubble and geometry constriction width restricts the skyrmion bubble forming in a line chain (Figure 2b–d). The corresponding micromagnetic simulation confirms the generation evolution by highlighting the clear shift of the SRT domain interface between the *c*-axis and *a*–*b* plane magnetization (Figure 2e–h). More strikingly, owing to the rigid edge confinement, the skyrmion bubble chains can also be created and stabilized via electron-assisted control in the absence of an external

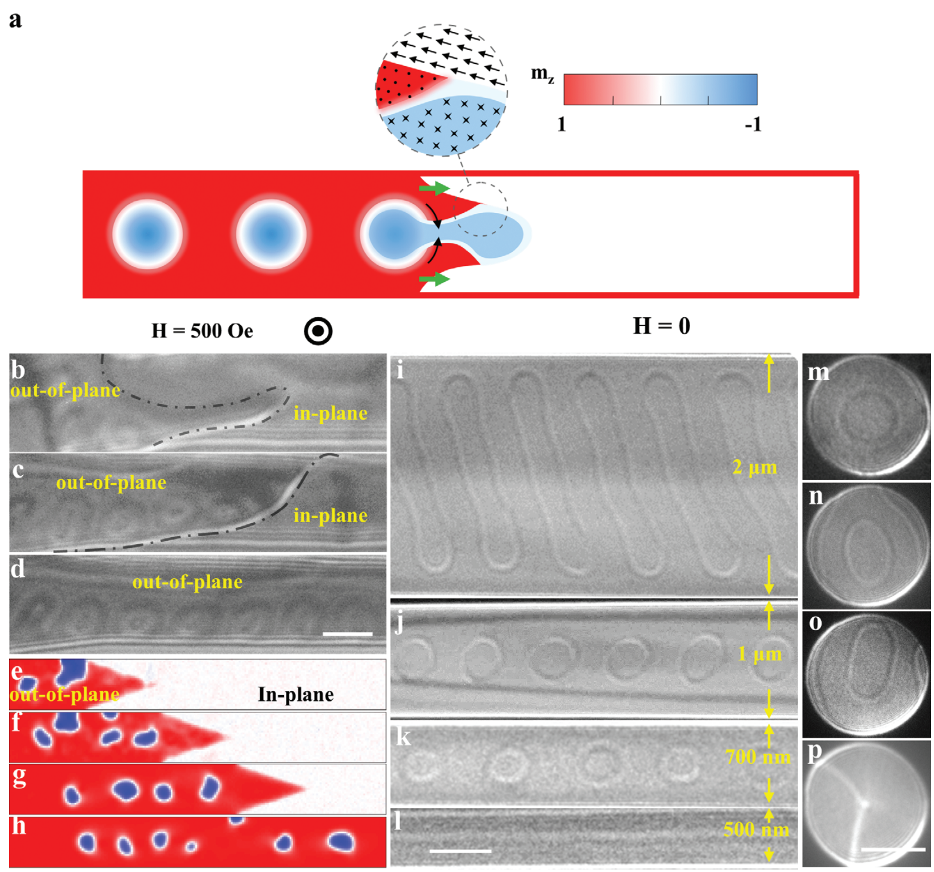

Figure 2. Skyrmion bubble generated via converging electron beam near SRT domain interface in a confined geometry with (left side) and without (right side) magnetic field. a) Schematic illustration of the skyrmion bubble generation from dynamic shifting and squeezing the SRT domain interface in a narrow prototype device. b–d) Skyrmion bubble chain generated via converging the electron beam under the same perpendicular magnetic field of 500 Oe but with edge confinement on both sides. The local SRT domain interface with anisotropy between the *c*-axis and *a–b* plane is marked with a black dot line. e–h) Corresponding simulated domain evolution by OOMMF, manifesting the contribution of SRT domain interface. The magnetization along the *c*-axis is represented by red ($+m_z$) and blue ($-m_z$) with the white area for *a–b* plane magnetization. i–l) Skyrmion bubble chain at zero field due to the geometric edge confinement with different sample widths after using electron-assisted control. m–p) Different types of isolated bubbles (l–n) and vortex (o) inside the 1 µm diameter nanodisk at zero field after similar electron-assisted control. The scale bar is 500 nm.

field (Figure 2i,j). The dynamic process of bubble chain formation can be clearly observed in the narrow stripe widths of 1 µm while dispersing the focused beam (Video S2, Supporting Information). The dependence of domain configuration on the width of the sample at zero field demonstrates an elongated elliptic domain in a 2 µm wide stripe in comparison to the nearly-rounded skyrmion bubbles in the narrower stripe with a width of 1 µm and 700 nm (Figure 2i–k), respectively, emphasizing the confinement contribution from the sample edge. When the width narrows to ≈500 nm, only a long domain line remains along the stripe (Figure 2l) because the stripe sample is not wide enough to host skyrmion bubbles.

We further restrict the size in all directions by fabricating disks with a diameter of ≈1 µm, resulting in almost round skyrmion bubbles and type II bubbles (bubbles with a topological number of zero[61,62]) (Figure 2m–o). The slight deformation of bubbles in Figure 2n,o is due to the extrusion of residual stripe domains, indicating the confinement from the domain wall. When continuously converging the electron beam to above SRT temperature, individual vortices are created due to the completely-transformed *a–b* plane anisotropy (Figure 2p). Overall, we have shown that the skyrmion bubble chain and individual skyrmion bubble can be generated at zero field by utilizing the electron-assisted SRT domain interface in the edge-confined prototype device.

2.3. The Skyrmion Bubble Movement Actualized by Shifting the SRT Domain Interface

Using electric-driven topological magnetic texture movement to transport information offers significant advantages in terms of energy efficiency and information stability for advanced spintronics applications. However, the usual pinning effects and skyrmion Hall effect limits their straight and efficient movements in ferromganets.[25–28] Here, we demonstrate the straight skyrmion bubble movement by shifting the SRT domain interface with skyrmion bubble slaved to form an elastic composite object (**Figure 3**), avoiding the free-skyrmion deflection from the skyrmion Hall effect. We create an isolated single skyrmion bubble by increasing the perpendicular field to ≈1320 Oe in the confined 1 µm channel (Figure 3a) to simplify the response of the skyrmion bubble lattice (Note S4, Video S3, Supporting

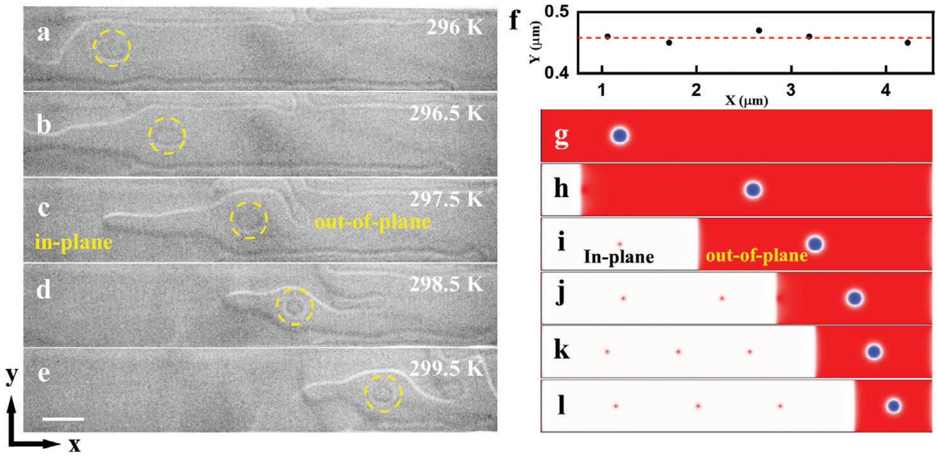

Figure 3. Straight movement of an individual skyrmion bubble by shifting the SRT domain interface with heating. a–e) L-TEM images of the skyrmion bubble movement while increasing temperature from 296 to 299.5 K to induce the SRT transition. f) Corresponding skyrmion bubble position along respective x and y directions at different temperatures without seeing significant transverse deviation. g–l) Micromagnetic simulation showing the skyrmion bubble movement with the shift of the SRT domain interface due to the local anisotropy change. The aspect ratio of the rectangular band is set as 7.5. The magnetization along the c-axis is represented by red ($+m_z$) and blue ($-m_z$) with the a–b plane magnetization by white color. The red spot represents the vortex core position in the background of the ab-plane anisotropy. The scale bar is 500 nm. The coordinate system with the x and y axes is shown.

Information). Subsequently, the expansion of the a–b plane domain due to temperature-induced SRT leads to the continuous shift of the domain interface along a straight line (Figure 3a-e, together with Video S4 in Supporting Information). The scale of the elastic composite object with skyrmion bubble slaved to the SRT domain interface is easier to smear out the random pinning potential. By this way, the skyrmion bubble with opposite chirality and even topologically trivial type II bubble can also be transported together with the SRT domain interface along a straight line (Notes S5,S6, together with Video S5, Supporting Information). The quantified displacement in respective x and y direction during its movement in Figure 3f demonstrates an almost straight trajectory without significant deviation along the y direction. Note that the transported bubble would not return back with the domain interface while removing the heating source (Supporting Notes S5,S7, Supporting Information), indicating the directional capability of carrying information.

The corresponding micromagnetic simulations are conducted with an individual skyrmion bubble inside the dominant c-axis magnetization as an initial state. Gradually changing the anisotropy from the c-axis to the a–b plane results in a similar shift of the SRT domain interface to the right, which simultaneously pushes the skyrmion bubble as a composite object due to the repulsion of DDI interactions (Figure 3g–l). Simulation results confirm the straight movement of both the skyrmion bubble and the type II bubble along the central line without any deviation in the y direction (Note S8, Supporting Information).

2.4. The Straight Skymrion Bubble Movement via Shifting SRT Domain Interface with In-Plane Electric Current Pulse

Importantly, the skyrmion bubble-driven movement via shifting SRT domain interface can be conveniently conducted by manipulating electron beam (Note S6, Supporting Information) and electric current, thereby properly addressing the practical challenges associated with common heating. Here, every time only one square pulse with a pulse width of 100 ns is loaded. Interestingly, the reversed electric current direction from **Figure** 4a–g as marked by the respective red and blue arrow yields the same movement direction of type II bubble from left to right, which excludes the STT effects[63,64] and distinguishes from the expected annihilation for the topologically trivial spin texture with topological number 0.[65]

To better understand the unique phenomena, the relationship between the extracted temperature and the waveform of the electric pulse is summarized from the middle part of the sample (Figure 4h) based on COMSOL temperature simulation with the same amplitude and pulse width of the current (10 mA and 100 ns) (Note S9, Supporting Information). It turns out that the pulsed current can increase the sample to a maximum temperature of 298.3 K, which is sufficient to shift the SRT domain interface with the skyrmion bubble as a composite object as shown in Figure 3. Four representative domain evolution states as marked in Figure 4h are schematically illustrated (Figure 4i–l) to represent the intermediate dynamic behavior during the time period of 500 ns. The dynamic process is similar to the temperature-induced behavior (Figure 3a–d) by shifting the SRT domain interface with the type II bubble as a composite object, not a free particle. Decreasing the current amplitude would change the magnetization back to the c-axis with the simultaneous return of the domain interface, leaving the bubble behind (Figure 4l). The fast dynamic process ≈400 ns is shorter than the time resolution of the charge-coupled device (CCD) used for image recording. Therefore, only the final state (Figure 4l) after one current pulse can be recorded in L-TEM images.

Therefore, the electric current can be used as a convenient heating source to drive the local anisotropy change and push the skyrmion bubble move forward with the SRT domain interface as an elastic composite object. The higher pulse current density drives the skyrmion bubble to a further distance (Figures 4a–d) due to the faster-increased temperature. The

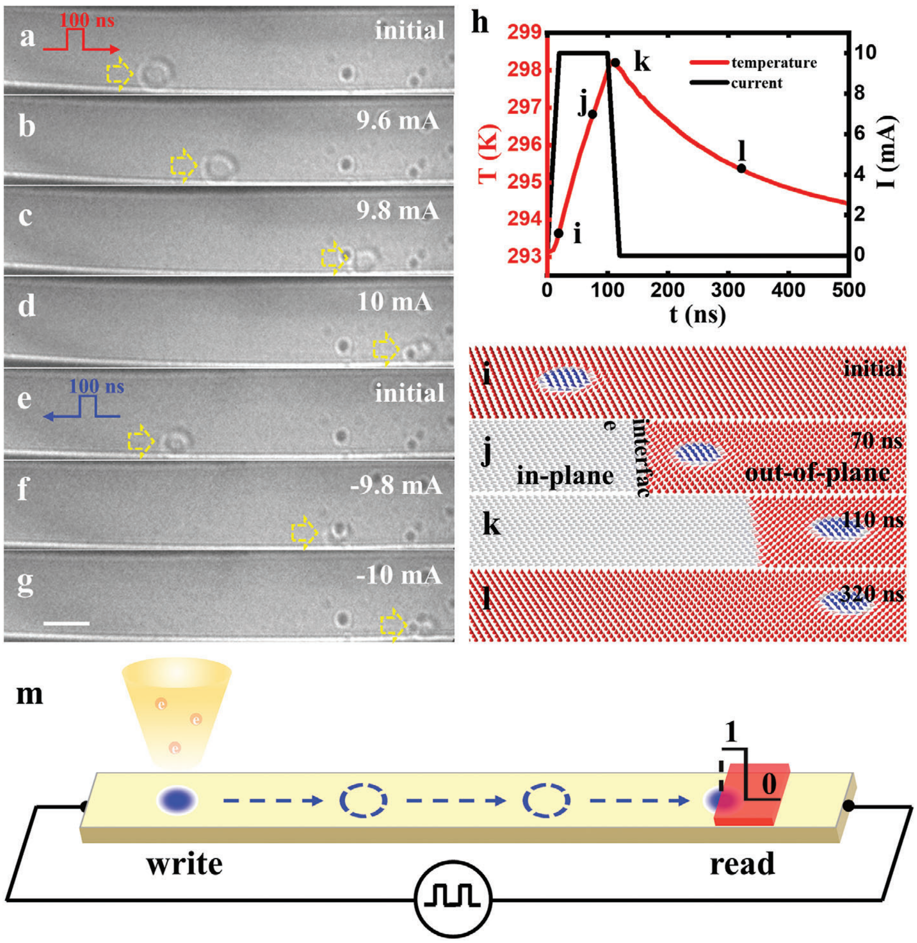

Figure 4. Straight movement of an individual type II bubble driven by pulsed electric current at 294 K. A perpendicular field of 1340 Oe is applied to obtain a single isolated bubble. a–d) Current-driven movement of type II bubble along the $+x$ direction after one pulse current with 100 ns width. e–g) Bubble movement under the same current magnitude but reversed direction. The amplitude and direction of the pulse current is marked out. h) Relationship between the pulse profile and the simulated sample temperature extracted by COMSOL. i–l) Schematic spin configuration evolution revealing the dynamic intermediate state during the pulse excitation. Red ($+m_z$) and blue ($-m_z$) denote the magnetization direction along the *c*-axis while white region denotes *a–b* plane magnetization. m) Schematic design of skyrmionic devices based on electron-assisted generation and transportation. The scale bar is 500 nm.

approximate velocity is calculated to be $\approx$30 m s^{-1} under the current density of ($j_e \approx 10^9$ A m^{-2}) in Note S10 (Supporting Information), which is comparable to the speed of STT-driven skyrmions motion at similar current density ($j_e \approx 10^{10}$ A m^{-2}).[25,27,63] Moreover, such a current-driven behavior could be also applicable for different spin textures such as skyrmion, type II bubble, and skyrmion bubbles (Note S11, Supporting Information) with straight trajectory. By conveniently utilizing the electron-assisted local anisotropy change near the SRT domain interface, information can be written from converging electron beam and subsequently transported via applying electric current in prototype devices as schematically shown in Figure 4m.

3. Conclusion

In this study, we have experimentally demonstrated the electron intensity gradient by conveniently converging the electron beam can dynamically oscillate and squeeze out the skyrmion bubble at room temperature near the SRT domain interface, which is subsequently driven along a straight trajectory with the skyrmion bubble integrated as an elastic composite object, overcoming the challenges from typical pinning and lateral deflection for skyrmions in ferromagnetic background. The corresponding micromagnetic simulations confirm the crucial contribution of local anisotropy variation near the SRT domain interface and geometric confinement in stabilizing and transporting the skyrmion bubbles. The concrete demonstration and comprehensive understanding of skyrmion bubble generation and movement with convenient electron-assisted control approaches in quantum $TbMn_6Sn_6$ at room temperature represents a significant step forward for the compatible application of topological textures in skyrmionic devices.

4. Experimental Section

Sample Synthesis and Characterization: The single crystals of $TbMn_6Sn_6$ synthesized by the self-flux method were the same as that used in the previous work.[66] Bruker D8 X-ray diffractometer with Cu K_α radiation ($\lambda = 0.15\,418$ nm) was used to obtain single crystal X-ray diffraction patterns at room temperature. Magnetization measurements were performed in Quantum Design MPMS3.

L-TEM Measurements: JEOL-dedicated L-TEM (JEOL2100F) was used to observe the domain evolution in $TbMn_6Sn_6$. The high-temperature manipulation was carried on by Double Tilt Heating Holder (Gatan 652 TA). The Keithley 4200A-SCS electrical measurement system was established to apply pulsed current via Double Tilt Thermoelectrical Holder. The magnetic field perpendicular to the sample plane was tuned by objective lens current. The in-plane magnetization deflected the incident electron beam and brought out the domain wall contrast under the convergent or divergent electron beam. The images with under-focal lengths were captured by a CCD camera with an exposure time of 0.2 s. The selected-area electron diffraction was applied to calibrate the crystalline orientation for grains. The specimens with special design along (001) zone-axis for L-TEM observation were prepared via focus ion beam milling and patterning. The constrained tunnel sample with the desired width was fabricated from the *ab*-plane of $TbMn_6Sn_6$ single crystal.

Micromagnetic Simulation: Micromagnetic simulations were performed using the standard OOMMF extensible solver (OXS).[60] The energy terms considered in this simulation can be expressed as:

$$\varepsilon_{tot} = A \sum_i (\nabla \boldsymbol{m}_i)^2 - K \sum_i (m_i^z)^2 - H_z \sum_i m_i^z + \varepsilon_{dem} \tag{1}$$

where m_i represents the local moment reduced by saturation magnetization M_s at the site i, A is the exchange stiffness, K is the perpendicular magnetic anisotropy constant, H_z is the perpendicular magnetic field and ϵ_{dem} is the energy density for demagnetization. The demagnetization energy term computed the average demagnetization field in each mesh cell using formulae from Refs. [67,68] and convolution via the Fast Fourier Transform. DMI was absent in this model for the centrosymmetric crystal structure of $TbMn_6Sn_6$. Since a massive computational time was required with experimental length scale in micromagnetic simulation, for convenience, the parameters for smaller skyrmions were chosen in a small simulation area (1.2 µm × 1.2 µm × 5 nm). The mesh size was $2 \times 2 \times 5$ nm^3, which was much smaller than the typical exchange length and the skyrmion size, to ensure a balance between numerical accuracy and computational efficiency. The parameters were set as $A = 5$ pJ m^{-1}, $K_u = 4 \times 10^5$ J m^{-3} for out-of-plane anisotropy and $K_u = -1 \times 10^3$ J m^{-3} for in-plane anisotropy, $M_s = 800 \times 10^3$ A m^{-1}, $H_z = 200$ Oe, $\alpha = 0.014$, where the saturation magnetization and out-of-plane anisotropy constant was higher and the perpendicular field was lower than the experimental parameters in order to match the numbers of the stripe domains in the reduced domain size. The value of the perpendicular magnetic field was not enough to convert the stripe domains into bubbles. To simulate the tunnel in this experiment, the width of the simulated area was reduced to 0.16 µm with the periodic boundary condition in length, and a higher magnetic field of 300 Oe was used to stabilize the bubble in this case. The Xf_ThermSpinXfer evolver was used to simulate the spin relaxation after fluctuation and the CG evolver was used to simulate the domain-wall-driven behavior.

COMSOL Multiphysics Simulation: Time-dependent temperature variation of the samples was simulated by using COMSOL Multiphysics software. The module used in this simulation was "Joule Heating" which included an "Electric Currents" interface, a "Heat Transfer in Solids" interface, and a Multiphysics node (Electromagnetic Heating). Time-Dependent Solver was chosen to study the temperature evolution during the pulsed current. The simulated structure consisted of three parts: the Si_3N_4 substrate, the Pt electrodes with a thickness of 1 µm, and $TbMn_6Sn_6$ lamina. They were labeled with the colors brown, orange, and yellow respectively. A region of 7×1 µm^2 in the middle of the stripe was thinned to 200 nm to form a constrained tunnel and the region in the surrounding had a thickness of 1 µm. All the parameters needed in the COMSOL simulations are listed in Table Supporting Information of Note S9 (Supporting Information).

Supporting Information

Supporting Information is available from the Wiley Online Library or from the author.

Acknowledgements

This work was supported by the Science Centre of the National Science Foundation of China (Grant No. 52088101), the Strategic Priority Research Program of the Chinese Academy of Sciences (Grant no. XDB33030100), the National Natural Science Foundation of China (Nos. 52271195, 11822412, 52130103, 51925605, 11774423, 12274459), the CAS Project for Young Scientists in Basic Research No. YSBR-084, National Key R&D Program of China (Grant Nos. 2018YFE0202600, 2022YFA1403800), Beijing Natural Science Foundation (Grant No. Z200005), Beijing National Laboratory for Condensed Matter Physics. The work at LANL was carried out under the auspices of the U.S. DOE NNSA under contract No. 89233218CNA000001 through the LDRD Program, and was performed, in part, at the Center for Integrated Nanotechnologies, an Office of Science User Facility operated for the U.S. DOE Office of Science, under user proposals #2018BU0010 and #2018BU0083.

Conflict of Interest

The authors declare no conflict of interest.

Author Contributions

Y.Z. and B.G.S. supervised the project. Q.W.Y., W.X.L., and H.C.L. synthesized the single crystals and carried out structural characterization and magnetization measurements; Z.L.L. and Y.Z. performed magnetic domain and dynamic behaviour experiments via Lorentz TEM. Z.L.L., Q.W.Y., H.C.L., and Y.Z. analysed the experimental data and plotted the figures; Z.L.L. and S.Z.L. did the simulation work; Z.L.L., S.Z.L., and Y.Z. wrote the manuscript after discussing data with H.C.L., J. S., S.G.W., J.W.C., T.Y.Z., B.G.S., and all the authors.

Data Availability Statement

The data that support the findings of this study are available from the corresponding author upon reasonable request.

Keywords

electron-assisted control, Kagome $TbMn_6Sn_6$, skyrmion bubble, SRT domain interface, topological domains

Received: September 15, 2023
Revised: December 31, 2023
Published online:

[1] S. Mühlbauer, B. Binz, F. Jonietz, C. Pfleiderer, A. Rosch, A. Neubauer, R. Georgii, P. Böni, *Science* **2009**, *323*, 915.
[2] X. Z. Yu, Y. Onose, N. Kanazawa, J. H. Park, J. H. Han, Y. Matsui, N. Nagaosa, Y. Tokura, *Nature* **2010**, *465*, 901.
[3] X. Z. Yu, N. Kanazawa, Y. Onose, K. Kimoto, W. Z. Zhang, S. Ishiwata, Y. Matsui, Y. Tokura, *Nat. Mater.* **2011**, *10*, 106.
[4] C. Moreau-Luchaire, C. Moutafis, N. Reyren, J. Sampaio, C. A. F. Vaz, N. Van Horne, K. Bouzehouane, K. Garcia, C. Deranlot, P. Warnicke, P. Wohlhüter, J.-M. George, M. Weigand, J. Raabe, V. Cros, A. Fert, *Nat. Nanotechnol.* **2016**, *11*, 444.

[5] H. Yang, A. Thiaville, S. Rohart, A. Fert, M. Chshiev, *Phys. Rev. Lett.* **2015**, *115*, 267210.
[6] F. Büttner, I. Lemesh, G. S. D. Beach, *Sci. Rep.* **2018**, *8*, 4464.
[7] S. A. Montoya, S. Couture, J. J. Chess, J. C. T. Lee, N. Kent, D. Henze, S. K. Sinha, M.-Y. Im, S. D. Kevan, P. Fischer, B. J. McMorran, V. Lomakin, S. Roy, E. E. Fullerton, *Phys. Rev. B* **2017**, *95*, 024415.
[8] S. A. Montoya, S. Couture, J. J. Chess, J. C. T. Lee, N. Kent, M.-Y. Im, S. D. Kevan, P. Fischer, B. J. McMorran, S. Roy, V. Lomakin, E. E. Fullerton, *Phys. Rev. B* **2017**, *95*, 224405 .
[9] T. Kurumaji, T. Nakajima, M. Hirschberger, A. Kikkawa, Y. Yamasaki, H. Sagayama, H. Nakao, Y. Taguchi, T.-H. Arima, Y. Tokura, *Science* **2019**, *365*, 914.
[10] M. Hirschberger, T. Nakajima, S. Gao, L. Peng, A. Kikkawa, T. Kurumaji, M. Kriener, Y. Yamasaki, H. Sagayama, H. Nakao, K. Ohishi, K. Kakurai, Y. Taguchi, X. Yu, T.-H. Arima, Y. Tokura, *Nat. Commun.* **2019**, *10*, 5831.
[11] Z. Wang, Y. Su, S. Z. Lin, C. D. Batista, *Phys. Rev. Lett.* **2020**, *124*, 207201.
[12] T. Okubo, S. Chung, H. Kawamura, *Phys. Rev. Lett.* **2012**, *108*, 017206.
[13] S.-Z. Lin, S. Hayami, *Phys. Rev. B* **2016**, *93*, 064430.
[14] A. O. Leonov, M. Mostovoy, *Nat. Commun.* **2015**, *6*, 8275.
[15] Y. Guang, I. Bykova, Y. Liu, G. Yu, E. Goering, M. Weigand, J. Gräfe, S. K. Kim, J. Zhang, H. Zhang, Z. Yan, C. Wan, J. Feng, X. Wang, C. Guo, H. Wei, Y. Peng, Y. Tserkovnyak, X. Han, G. Schütz, *Nat. Commun.* **2020**, *11*, 949.
[16] S.-G. Je, P. Vallobra, T. Srivastava, J.-C. Rojas-Sánchez, T. H. Pham, M. Hehn, G. Malinowski, C. Baraduc, S. Auffret, G. Gaudin, S. Mangin, H. Béa, O. Boulle, *Nano Lett.* **2018**, *18*, 7362.
[17] N. Romming, C. Hanneken, M. Menzel, J. E. Bickel, B. Wolter, K. von Bergmann, A. Kubetzka, R. Wiesendanger, *Science* **2013**, *341*, 636.
[18] Y. Guang, Y. Peng, Z. Yan, Y. Liu, J. Zhang, X. Zeng, S. Zhang, S. Zhang, D. M. Burn, N. Jaouen, J. Wei, H. Xu, J. Feng, C. Fang, G. van der Laan, T. Hesjedal, B. Cui, X. Zhang, G. Yu, X. Han, *Adv. Mater.* **2020**, *32*, 2003003.
[19] K. Hamamoto, M. Ezawa, N. Nagaosa, *Phys. Rev. B* **2015**, *92*, 115417.
[20] T. Schulz, R. Ritz, A. Bauer, M. Halder, M. Wagner, C. Franz, C. Pfleiderer, K. Everschor, M. Garst, A. Rosch, *Nat. Phys.* **2012**, *8*, 301.
[21] J. Iwasaki, M. Mochizuki, N. Nagaosa, *Nat. Commun.* **2013**, *4*, 1463.
[22] A. Fert, N. Reyren, V. Cros, *Nat. Rev. Mater.* **2017**, *2*, 17031.
[23] A. Fert, V. Cros, J. Sampaio, *Nat. Nanotechnol.* **2013**, *8*, 152.
[24] S.-Z. Lin, C. Reichhardt, C. D. Batista, A. Saxena, *Phys. Rev. B* **2013**, *87*, 214419.
[25] W. Jiang, X. Zhang, G. Yu, W. Zhang, X. Wang, M. Benjamin Jungfleisch, J. E. Pearson, X. Cheng, O. Heinonen, K. L. Wang, Y. Zhou, A. Hoffmann, S. G. E. te Velthuis, *Nat. Phys.* **2016**, *13*, 162.
[26] N. Nagaosa, Y. Tokura, *Nat. Nanotechnol.* **2013**, *8*, 899.
[27] K. Litzius, I. Lemesh, B. Krüger, P. Bassirian, L. Caretta, K. Richter, F. Büttner, K. Sato, O. A. Tretiakov, J. Förster, R. M. Reeve, M. Weigand, I. Bykova, H. Stoll, G. Schütz, G. S. D. Beach, M. Kläui, *Nat. Phys.* **2017**, *13*, 170.
[28] C. Reichhardt, C. J. O. Reichhardt, M. V. Milošević, *Rev. Mod. Phys.* **2022**, *94*, 035005.
[29] J. Mulkers, B. Van Waeyenberge, M. V. Milošević, *Phys. Rev. B* **2017**, *95*, 144401.
[30] S. Yang, K. Wu, Y. Zhao, X. Liang, J. Xia, Y. Zhou, X. Xing, Y. Zhou, *Phys. Rev. Appl.* **2022**, *18*, 024030.
[31] R. Chen, C. Chen, L. Han, P. Liu, R. Su, W. Zhu, Y. Zhou, F. Pan, C. Song, *Nat. Commun.* **2023**, *14*, 4427.
[32] Z. Wang, M. Guo, H.-A. Zhou, L. Zhao, T. Xu, R. Tomasello, H. Bai, Y. Dong, S.-G. Je, W. Chao, H.-S. Han, S. Lee, K.-S. Lee, Y. Yao, W. Han, C. Song, H. Wu, M. Carpentieri, G. Finocchio, M.-Y. Im, S.-Z. Lin, W. Jiang, *Nat. Electron.* **2020**, *3*, 672.
[33] Y. Hirata, D.-H. Kim, S. K. Kim, D.-K. Lee, S.-H. Oh, D.-Y. Kim, T. Nishimura, T. Okuno, Y. Futakawa, H. Yoshikawa, A. Tsukamoto, Y. Tserkovnyak, Y. Shiota, T. Moriyama, S.-B. Choe, K.-J. Lee, T. Ono, *Nat. Nanotechnol.* **2019**, *14*, 232.
[34] J. Barker, O. A. Tretiakov, *Phys. Rev. Lett.* **2016**, *116*, 147203.
[35] T. Dohi, S. DuttaGupta, S. Fukami, H. Ohno, *Nat. Commun.* **2019**, *10*, 5153.
[36] R. Chen, Q. Cui, L. Han, X. Xue, J. Liang, H. Bai, Y. Zhou, F. Pan, H. Yang, C. Song, *Adv. Funct. Mater.* **2022**, *32*, 2111906.
[37] E. Tang, J. W. Mei, X. G. Wen, *Phys. Rev. Lett.* **2011**, *106*, 236802.
[38] C. Wu, D. Bergman, L. Balents, S. D. Sarma, *Phys. Rev. Lett.* **2007**, *99*, 070401.
[39] M. Kang, L. Ye, S. Fang, J.-S. You, A. Levitan, M. Han, J. I. Facio, C. Jozwiak, A. Bostwick, E. Rotenberg, M. K. Chan, R. D. McDonald, D. Graf, K. Kaznatcheev, E. Vescovo, D. C. Bell, E. Kaxiras, J. van den Brink, M. Richter, M. Prasad Ghimire, J. G. Checkelsky, R. Comin, *Nat. Mater.* **2020**, *19*, 163.
[40] Z. Hou, Q. Zhang, X. Zhang, G. Xu, J. Xia, B. Ding, H. Li, S. Zhang, N. M. Batra, P. M. F. J. Costa, E. Liu, G. Wu, M. Ezawa, X. Liu, Y. Zhou, X. Zhang, W. Wang, *Adv. Mater.* **2020**, *32*, 1904815.
[41] W. Wei, J. Tang, Y. Wu, Y. Wang, J. Jiang, J. Li, Y. Soh, Y. Xiong, M. Tian, H. Du, *Adv. Mater.* **2021**, *33*, 2101610.
[42] Z. Hou, W. Ren, B. Ding, G. Xu, Y. Wang, B. Yang, Q. Zhang, Y. Zhang, E. Liu, F. Xu, W. Wang, G. Wu, X. Zhang, B. Shen, Z. Zhang, *Adv. Mater.* **2017**, *29*, 1701144.
[43] M. Pereiro, D. Yudin, J. Chico, C. Etz, O. Eriksson, A. Bergman, *Nat. Commun.* **2014**, *5*, 4815.
[44] B. Malaman, G. Venturini, R. Welter, J. P. Sanchez, P. Vulliet, E. Ressouche, *J. Magn. Magn. Mater.* **1999**, *202*, 519.
[45] D. Clatterbuck, K. Gschneidner, *J. Magn. Magn. Mater.* **1999**, *207*, 78.
[46] X. Yu, M. Mostovoy, Y. Tokunaga, W. Zhang, K. Kimoto, Y. Matsui, Y. Kaneko, N. Nagaosa, Y. Tokura, *Proc. Natl. Acad. Sci. USA* **2012**, *109*, 8856.
[47] Y. Yao, B. Ding, J. Liang, H. Li, X. Shen, R. Yu, W. Wang, *Nat. Commun.* **2022**, *13*, 5991.
[48] I. Makhfudz, B. Krüger, O. Tchernyshyov, *Phys. Rev. Lett.* **2012**, *109*, 217201.
[49] X. Z. Yu, K. Shibata, W. Koshibae, Y. Tokunaga, Y. Kaneko, T. Nagai, K. Kimoto, Y. Taguchi, N. Nagaosa, Y. Tokura, *Phys. Rev. B* **2016**, *93*, 134417.
[50] M. Ezawa, *Phys. Rev. Lett.* **2010**, *105*, 197202.
[51] D. B. Williams, C. B. Carter, *Transmission Electron Microscope: a textbook for materials science*, Springer, New York **2009**, Vol. *74*.
[52] T. Yokota, M. Murayama, J. M. Howe, *Phys. Rev. Lett.* **2003**, *91*, 265504.
[53] X. Yu, D. Morikawa, Y. Tokunaga, M. Kubota, T. Kurumaji, H. Oike, M. Nakamura, F. Kagawa, Y. Taguchi, T.-H. Arima, M. Kawasaki, Y. Tokura, *Adv. Mater.* **2017**, *29*, 1606178.
[54] J. Sampaio, V. Cros, S. Rohart, A. Thiaville, A. Fert, *Nat. Nanotechnol.* **2013**, *8*, 839.
[55] S. Zuo, J. Liu, K. Qiao, Y. Zhang, J. Chen, N. Su, Y. Liu, J. Cao, T. Zhao, J. Wang, F. Hu, J. Sun, C. Jiang, B. Shen, *Adv. Mater.* **2021**, *33*, 2103751.
[56] V. Kumar, N. Kumar, M. Reehuis, J. Gayles, A. S. Sukhanov, A. Hoser, F. Damay, C. Shekhar, P. Adler, C. Felser, *Phys. Rev. B* **2020**, *101*, 014424.
[57] Z. Li, J. Su, S.-Z. Lin, D. Liu, Y. Gao, S. Wang, H. Wei, T. Zhao, Y. Zhang, J. Cai, B. Shen, *Nat. Commun.* **2021**, *12*, 5604.
[58] Y. Gao, Q. Yin, Q. Wang, Z. Li, J. Cai, T. Zhao, H. Lei, S. Wang, Y. Zhang, B. Shen, *Adv. Mater.* **2020**, *32*, 2005228.
[59] J. Leliaert, M. Dvornik, J. Mulkers, J. De Clercq, M. V. Milosevic, B. Van Waeyenberge, *J. Phys. D: Appl. Phys.* **2018**, *51*, 123002.
[60] M. J. Donahue, D. G. Porter, OOMMF User's Guide, Version 1.0. (Interagency Report NISTIR 6376, 1999), OOMMF User's Guide, Version 1.0. National Institute of Standards and Technology, Gaithersburg, MD, 1999, M. J. Donahue, D. G. Porter, OOMMF User's Guide, Version 1.0. (Interagency Report NISTIR 6376, 1999).

[61] D. Chakrabartty, S. Jamaluddin, S. K. Manna, A. K. Nayak, *Commun. Phys.* **2022**, *5*, 189.
[62] J. C. Loudon, A. C. Twitchett-Harrison, D. Cortés-Ortuño, M. T. Birch, L. A. Turnbull, A. Stefancic, F. Y. Ogrin, E. O. Burgos-Parra, N. Bukin, A. Laurenson, H. Popescu, M. Beg, O. Hovorka, H. Fangohr, P. A. Midgley, G. Balakrishnan, P. D. Hatton, *Adv. Mater.* **2019**, *31*, 1806598.
[63] S. Woo, K. Litzius, B. Krüger, M.-Y. Im, L. Caretta, K. Richter, M. Mann, A. Krone, R. M. Reeve, M. Weigand, P. Agrawal, I. Lemesh, M.-A. Mawass, P. Fischer, M. Kläui, G. S. D. Beach, *Nat. Mater.* **2016**, *15*, 501.
[64] L. Peng, K. Karube, Y. Taguchi, N. Nagaosa, Y. Tokura, X. Yu, *Nat. Commun.* **2021**, *12*, 6797.
[65] W. Jiang, P. Upadhyaya, W. Zhang, G. Yu, M. B. Jungfleisch, F. Y. Fradin, J. E. Pearson, Y. Tserkovnyak, K. L. Wang, O. Heinonen, S. G. E. te Velthuis, A. Hoffmann, *Science* **2015**, *349*, 283.
[66] Z. Li, Q. Yin, Y. Jiang, Z. Zhu, Y. Gao, S. Wang, J. Shen, T. Zhao, J. Cai, H. Lei, S.-Z. Lin, Y. Zhang, B. Shen, *Adv. Mater.* **2023**, *22*, 2211164.
[67] A. Aharoni, *J. Appl. Phys.* **1998**, *83*, 3432.
[68] A. J. Newell, W. Williams, D. J. Dunlop, *J. Geophys. Res. Solid Earth* **1993**, *98*, 9551.